



Polarization-dependent center-of-mass motion of an optically levitated nanosphere

YUANBIN JIN,¹ XUDONG YU,^{1,2} AND JING ZHANG^{1,3}

¹The State Key Laboratory of Quantum Optics and Quantum Optics Devices, Institute of Opto-Electronics, Synergetic Innovation Center of Quantum Information and Quantum Physics, Shanxi University, Taiyuan 030006, China

²e-mail: jjance_yu@sxu.edu.cn

³e-mail: jzhang74@yahoo.com

Received 24 May 2019; revised 11 July 2019; accepted 18 July 2019; posted 19 July 2019 (Doc. ID 368308); published 7 August 2019

In this study, we report the influence on the center-of-mass translational motion of a levitated nanosphere in the case of the combination of an elliptical polarization with an elliptical TEM₀₀-mode Gaussian beam. A fundamental-mode Gaussian laser with a slightly elliptical profile is focused using a high numerical aperture objective lens for trapping a nanosphere. The field distribution of the strongly focused laser in the focus region depends on its polarization according to vector diffraction theory. Therefore, the motion of the nanosphere depends on the relative orientation and ellipticity of the two ellipses' parameters. For a linearly polarized light field, the eigenfrequencies and corresponding power spectra of the radial motions change periodically with the rotation of the linear polarization direction relative to the orientation of the elliptical TEM₀₀-mode Gaussian beam. We further demonstrate that these effects could be enhanced or canceled by controlling the relative orientation and ellipticity of the two ellipses' parameters. This work provides a more flexible method for manipulating an optically levitated nanosphere. Furthermore, the above-mentioned effects can be used to evaluate a tightly focused laser using the motion of the nanosphere. © 2019 Optical Society of America

<https://doi.org/10.1364/JOSAB.36.002369>

1. INTRODUCTION

Optical levitation is a particle-trapping technique that uses the radiation pressure of light and has been an important platform in fundamental physical studies, quantum metrology, and quantum information processing since the first experiment conducted by Ashkin in 1970 [1]. On the atomic scale, a single trapped atom can be used to produce single photons and realize quantum logic gates [2,3]. For microscale and nanoscale systems, the translational motion of a levitated dielectric sphere has a high Q factor in high vacuum [4]. This system is extremely sensitive to certain changes and has been used to perform some highly precise measurements [5–7] and even was proposed to realize macroscopic quantum phenomena [8–10]. Recently, center-of-mass motion control, torsional motion, fast spin, and even transverse spin of optically levitated particles have been reported [11–21]. The temperature of center-of-mass motion was cooled to the micro-Kelvin region [14], rotational frequency of spin can approach the gigahertz range [22,23], and the trajectory radius of transverse spin was larger than 1 μm [21]. These studies provide an opportunity to explore the Casimir torque [24–26], quantum nature of gravity [27,28], and nonequilibrium statistical

mechanics [21]. Furthermore, for a system with an optically trapped diamond containing nitrogen-vacancy centers, it can be used to study symmetry-breaking dynamics [29].

The depth of the trapping potential is critical for the optical levitation technique, which requires a large gradient force, especially in the longitudinal direction. Consequently, the trapping laser is usually tightly focused using a large numerical aperture (NA) lens. Considering a linearly polarized laser beam is concentrated on a small focus point, paraxial approximation is not applicable, and simultaneously polarization must be taken into account because the longitudinal component of the field is no longer zero [30–32]. Theoretical methods of vector diffraction have been developed to solve these problems [30,31,33–35] and have been widely applied in high-resolution imaging [36], optical trapping [37], nanofabrication [38], and near-field optics [39]. These studies demonstrate that the field distribution of a strongly focused laser in the focus region is dependent on polarization [40,41]. Therefore, the field gradient and resulting center-of-mass motion of the particle trapped relies on polarization [15]. The transfer of spin angular momentum of circularly and elliptically polarized lasers to a nanoparticle can induce rotation of the nanoparticle [22,23]. Here, we focus primarily on the influence on the center-of-mass

translational motion of a spherical nanoparticle in the case of the combination of an elliptical polarization with an elliptical TEM₀₀-mode Gaussian beam. In our experiment, a TEM₀₀-mode Gaussian beam with a slightly elliptical profile is focused by an objective lens with NA = 0.95 for trapping a nanoparticle. It is demonstrated that some effects could be enhanced or canceled by controlling the relative orientation and ellipticity of the two ellipses' parameters. The frequencies and amplitudes of the motion signals change periodically with the rotation of the direction of linear polarization. With respect to a circularly polarized trapping light field, the radial eigenfrequencies are non-degenerate. However, the frequency difference can be eliminated by choosing an appropriate polarization for an elliptically polarized laser.

2. THEORETICAL ANALYSIS

Optical trapping with a single beam has a simple layout, and it is easy to manipulate [14,42,43]. In our experiment, we use a single laser to trap the nanosphere. Hence, here we just consider the single-trapping beam case. Figure 1(a) presents a schematic diagram of the strong focusing effect of a collimated linearly polarized light. The light propagates along the optical axis of a high NA lens. In this figure, α is the diffracted angle with $0 \leq \alpha < \alpha_0$ (α_0 is the solid angle of the focused light, defined as $\alpha_0 = \arcsin(\text{NA})$ in vacuum), β is the azimuth angle and $0 \leq \beta < 2\pi$, \vec{P}_0 (\vec{P}) and \vec{k}_0 (\vec{k}) are the polarization unit vector and wave vector before (after) the lens. The ray-tracing model illustrates the focus effect. The blue ray changes its propagation direction after the lens and bends to the optical axis. Therefore, the polarization vector (\vec{P}) after the lens can be decomposed

into three coordinate axes (x , y , and z) of the Cartesian coordinate system, and the power is then split into three parts. The point of intersection is the geometrical focus, which corresponds to the Abbe's sine condition. Thus, neglecting spherical aberration, the rays have the same phase at the geometrical focus and different phases in regions beyond the focus; this causes constructive and destructive interference for the components of the field and determines the intensity distribution in the focus region. Vector diffraction theory is generally used to solve the problem of an ideal Gaussian beam [34,35]. Several studies on the nonparaxial properties of an elliptical Gaussian beam have also been reported [44,45]. Here, we use the angular spectrum representation to study the intensity distribution and field gradient of an elliptical Gaussian laser in the focus region. Considering the energy conservation condition and using the Debye integral, the components of the electric field in the focus region can be written as follows [41,46]:

$$\vec{E}(r, \phi, z) = ic \int_0^{\alpha_0} \int_0^{2\pi} A_{\text{in}}(\alpha, \beta) C_M \begin{pmatrix} \vec{P}_{x_0} \\ \vec{P}_{y_0} \\ \vec{P}_{z_0} \end{pmatrix} \cdot e^{ik[z \cos(\alpha) + r \sin(\alpha) \cos(\beta - \phi)]} \sqrt{\cos(\alpha) \sin(\alpha)} d\alpha d\beta, \quad (1)$$

where r , ϕ , and z are cylindrical coordinates in the focus region, c is a constant, $(\vec{P}_{x_0}, \vec{P}_{y_0}, \vec{P}_{z_0})^T$ is the polarization matrix unit vector of the input beam, C_M is the transformation matrix of the aplanatic lens [41,46], and A_{in} is the incident field mode.

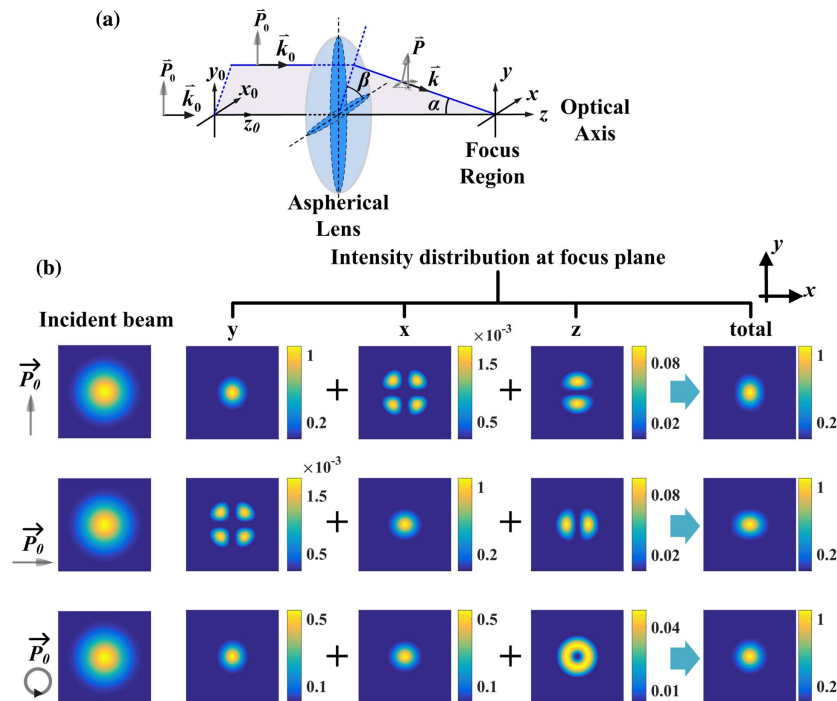


Fig. 1. Schematic diagram of the focus effect for a laser tightly focused using a high NA aplanatic lens. (a) Stereogram for linearly polarized light; (b) incident beam and focus plane intensity distribution. The first column refers to a circular TEM₀₀-mode Gaussian incident beam with different polarizations. The second to fifth columns refer to the corresponding intensity distributions of the y , x , z components, and the total, respectively. The x - and y -axes range from -2λ to 2λ .

Case 1: Circular profile of the incident field. First, we consider that the incident beam is a fundamental-mode Gaussian light beam with a circular profile, where A_{in} has a rotationally symmetric Gaussian amplitude distribution in angular spectrum representation. Detailed theoretical calculations are presented in the Appendix. Figure 1(b) illustrates the theoretical simulation of the radial intensity distribution in the focus region. If the polarization direction of a linearly polarized laser beam is parallel to the y_0 axis, the intensity distribution of the y component is slightly elliptical. This is because its zero-order term (related to the zero-order first-kind Bessel function) independent of the azimuthal angle (β) is slightly stretched by its small second-order term (related to the second-order first-kind Bessel function) along the y axis, which is a cosine function of 2β . The z component can be separated into two parts by the xz plane (i.e., one above and one below). The directions of the parts above and below are opposite one another, which causes destructive interference on the x axis and constructive interference beyond the xz plane. Consequently, the intensity distribution of the z component in the focus plane has a lobe structure along the y axis. For the x component, which is also a second-order term (a second-order first-kind Bessel function) and a sine function of 2β , the intensity distribution has four blades located in the four quadrants of the xy plane because of the destructive interference on the x and y axes. Therefore, the total intensity distribution in the xy plane, as the sum of the three components, is elongated along the polarization direction as the major axis of the total intensity distribution. However, the main energy component is in the y component, and the power ratio for the three components is $I_x:I_y:I_z \approx 0.0015:0.9:0.1$ for $NA = 0.95$. If the polarization is along the x_0 axis, the intensity distributions of the x and y components reverse, and the lobe structure of the z component becomes horizontal. Thus, the total radial intensity distribution is stretched along the x axis. In general, as the linear polarization direction is changed, the major axis of the total intensity distribution follows the polarization direction. However, the shape does not change because of the symmetry of the input field [Fig. 2(a)].

If the incident field is circularly polarized, the polarization can be split along the x_0 and y_0 axes with a fixed phase difference of $\pi/2$ or $-\pi/2$. Thus, the total intensity in the focus plane is the sum of the two individual parts, and the profile of the total intensity distribution in the xy plane is circular.

Case 2: Elliptical profile of the incident field. The profile of a fundamental-mode Gaussian beam in the experiment is actually not perfectly circular, but is usually elliptical, for instance, and is caused by noncollinearity of the lens, wavefront aberration originating from the uneven surfaces of the optical elements, and birefringence in the window of the vacuum chamber, and so on. Consequently, the mode of the incident field is not rotationally symmetric. We assume that the major axis of the elliptical incident beam is along the x_0 axis. The spot size of the incident beam along the y_0 axis is slightly reduced, and the size along the x_0 axis is unchanged relative to the circular incident beam discussed above. Therefore, we can define the ellipticity as $\delta = (w_{0x} - w_{0y})/w_{0x}$. If the ellipticity is very small ($\delta \ll 1$), the first-order approximation can be derived as presented in the Appendix. If the linear polarization direction is

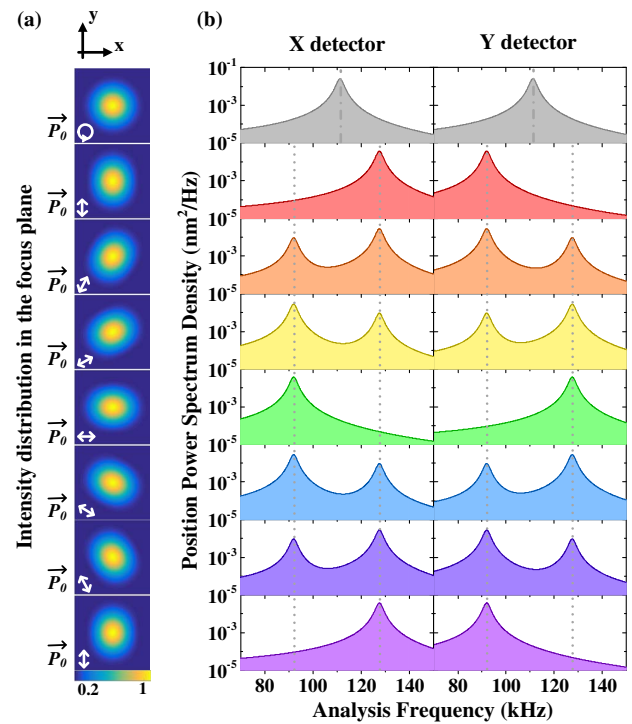


Fig. 2. (a) Theoretical calculation results of the intensity distributions in the focus plane for a circular TEM_{00} -mode Gaussian beam with different polarizations; (b) corresponding position spectral densities of the motions measured by the X and Y detectors, respectively. The dotted lines represent two eigenfrequencies for linear polarization, while the dotted-dashed lines represent the degenerate frequency for circular polarization. In the calculations, the power of the trapping laser is 50 mW, the NA of the aplanatic lens is 0.95, and the refractive index and density of the nanoparticle are 1.45 and 2.2 g/cm^3 .

along the y_0 axis, the total intensity distribution in the focus plane becomes longer along the y_0 axis than that of the circular incident beam. This effect is caused by two mechanisms, one in which the intensity distribution is stretched along the polarization direction mainly due to the longitudinal component, and the other, which involves the elliptical nature of the incident beam. In the case above, the ellipses induced by the two mechanisms are perfectly aligned. If the linear polarization direction is parallel to the x_0 axis, the total intensity profile in the xy plane becomes wider than in the case of circular incident light because the ellipses induced by the two mechanisms are orthogonal. Therefore, as the polarization direction is rotated, both the inclination angle and the shape of the radial intensity distribution are changed. Thus, the major axis of the radial intensity distribution is not always parallel to the polarization direction. If the polarization is circular, the intensity distribution in the focus plane is elliptical. Its major axis is parallel to the minor axis of the input beam, and its minor axis is parallel to the major axis of the input beam. A schematic diagram of the intensity distribution is presented in Fig. 3(a) for different polarizations.

The intensity distribution determines the field gradient. Here, the size of the silica nanosphere is smaller than the

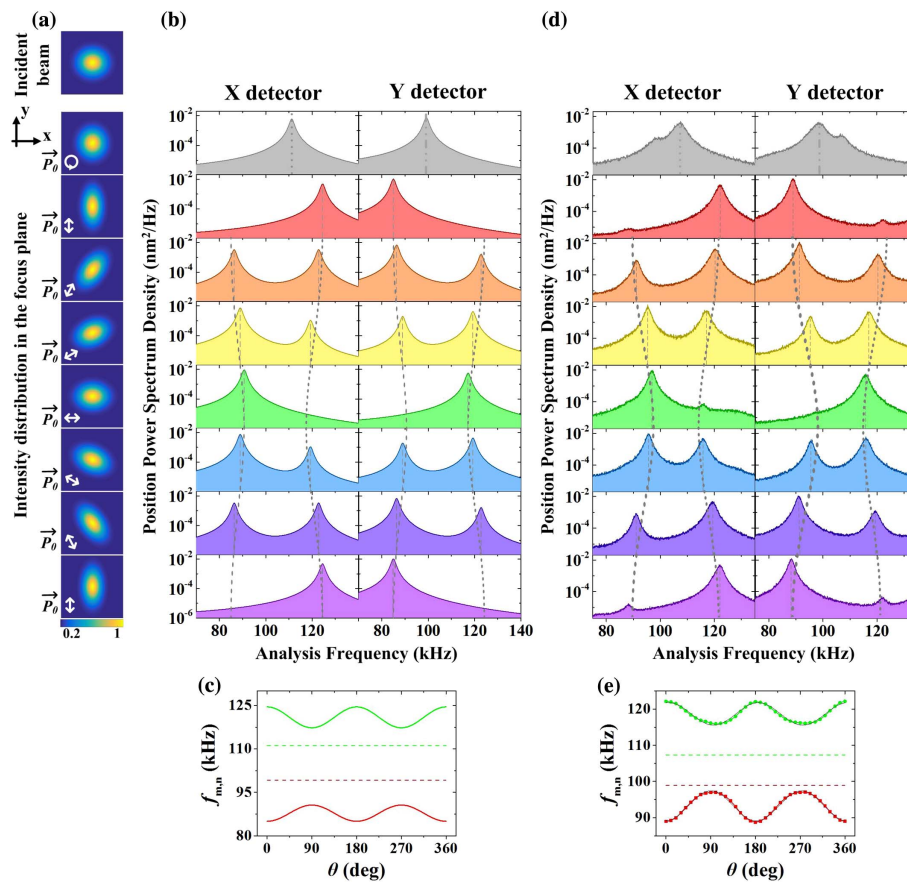


Fig. 3. (a)–(c) Theoretically calculated results. (a) Schematic diagram of the intensity distributions in the focus plane for an elliptical TEM₀₀-mode Gaussian beam with different polarizations. The ellipticity for input beam is 0.1 in the calculation. (b) Corresponding theoretical calculation results of the power spectral densities of the motions measured by the *X* and *Y* detectors. The dotted curves represent the theoretical simulations of the eigenfrequencies versus the rotation angle of the linearly polarized light field. The dotted and dotted-dashed straight lines correspond to the nondegenerate eigenfrequencies for the circularly polarized light field. (c) Radial eigenfrequencies versus θ . The green and red solid lines are the radial gradient force versus θ for a linearly polarized laser. The green and red dashed lines in the center represent the theoretically simulated results for a circularly polarized laser. The other parameters in the calculations are the same as Fig. 2. (d)–(e) Experimental results. (d) Power spectra measured by the position detectors *X* and *Y* versus θ for linearly and circularly polarized light fields; (e) radial eigenfrequencies. The top and bottom traces are periodically variational, corresponding to the experimental data (symbols) and theoretical fittings (solid lines) versus θ , respectively, for a linearly polarized laser. The green and red dashed lines in the center represent the results for a circularly polarized laser. The air pressure during the measurements was 300 Pa, the resolution bandwidth (RBW) was 10 Hz, and the video bandwidth (VBW) was 10 Hz.

wavelength, and the absorption can be neglected for a perfect dielectric sphere. Rayleigh approximation is thus suitable. In this case, the gradient force is larger than the scattering force, and the equilibrium position of the nanoparticle is located approximately at the geometrical focus. The restoring force is proportional to the field gradient and is linear near the focus point. Thus, the system can be seen as a harmonic oscillator in the small displacement approximation and is governed by a harmonic oscillation equation [47]. The field gradient can be derived by calculating the derivative of the intensity distribution function, as discussed in detail in Ref. [48]. For a circular fundamental-mode Gaussian light field, the radial intensity distribution in the focus plane has an ellipse-type profile for linear polarization. Consequently, the radial potential field near the focus has two eigendirections. One eigendirection is along the major axis of the intensity distribution ellipse. In this direction, the spring constant is at its minimum, which

corresponds to the minimum eigenfrequency of the center-of-mass translational motion. The other eigendirection is parallel to the minor axis and determines the maximum eigenfrequency. When the polarization is rotated, the intensity ellipse follows the rotation of the polarization direction, and the major axis remains parallel to the polarization direction. Thus, the corresponding eigenfrequencies of the trapped particle remain unchanged, but the directions of the motions follow the rotation of the polarization direction. Usually, the detection axes of the position detection systems in the experiment are fixed; thus, the position detectors *X* and *Y* in the radial direction can simultaneously measure two motion signals (the schematic diagram of projection measurement is shown in Fig. 4(b), and a brief formulaic expression is presented in next subsection). The eigenfrequencies remain unchanged, but the power spectrum heights of the signals are alternatively changed when the linear polarization direction is rotated [Fig. 2(b)].

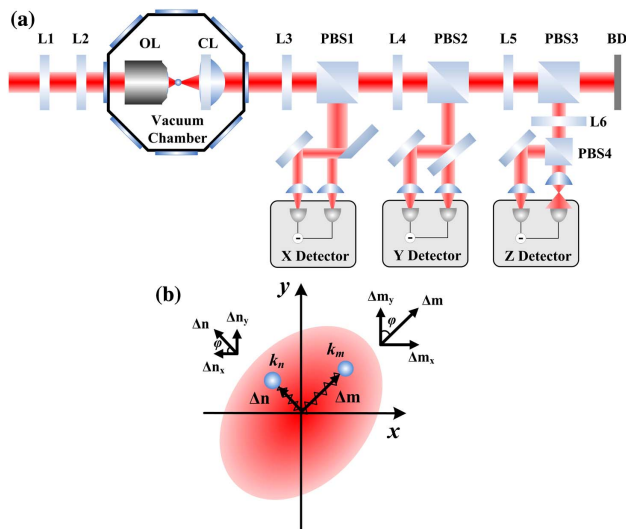


Fig. 4. (a) Schematic diagram of the experiment. Three pairs of position-sensitive detection systems measure the displacement of the x , y , and z dimensions. PBS 1-4, polarized beam splitters; L1, quarter-wave plate; L2-6, half-wave plates; OL, objective lens; CL, collimation lens; BD, block dump; (b) schematic diagram of the projection measurement.

Contrastingly, for a circularly polarized laser, the radial motions are degenerate because the intensity distribution is rationally symmetric and the position detectors obtain the same signal. If the input beam is an elliptical fundamental-mode Gaussian light field, the radial eigenfrequencies vary for different linear polarizations, and the radial eigendirection of the particle motion is not always parallel or perpendicular to the polarization direction. In the position measurement, the power spectra of the motion signals are changed when altering the linear polarization direction, which is quite different from the case of a circular Gaussian beam. The eigenfrequencies and their amplitudes in the power spectra are varied simultaneously, as shown in Fig. 3(b). For circular polarization, the two motional signals are no longer degenerate, and their frequencies are located in between two eigenfrequencies in the case of linear polarization.

3. EXPERIMENTAL SETUP AND RESULTS

Schematic diagrams of the experimental setup and projection measurement are presented in Figs. 4(a) and 4(b). A TEM₀₀-mode Gaussian 1064 nm light output from a diode-pumped single-frequency laser passed through a quarter- and half-wave plate to adjust the polarization. It was then tightly focused by an objective lens with NA = 0.95 to produce a harmonic potential field. The power of the 1064 nm laser was 50 mW. The strongly focused beam past the objective lens was collimated using another high NA lens. The two lenses were placed in a vacuum chamber. The droplets containing the nanoparticles were dispersed into the vacuum chamber by an ultrasonic nebulizer. A silica nanosphere with a radius of about 150 nm (the mass is about $m = 3.0 \times 10^{-14}$ g) was trapped. The output light from the chamber was divided into three parts for detecting the three-dimensional displacements. The transverse

displacements were measured via the D-shaped reflective mirrors. The position detectors utilizing a current subtraction circuit had a high common mode rejection ratio (CMRR). The current-voltage conversion gains were 10^4 and 3.3×10^3 for the X and Y detectors, respectively. Position detection is the projection measurement of the motion. Figure 4(b) presents a schematic diagram of the projection measurement in the radial direction. The X detector can simultaneously detect the projection Δn_x of a displacement Δn along the minor axis and the projection Δm_x of a displacement Δm along the major axis. Similarly, the Y detector can measure the displacement projections Δn_y and Δm_y . Thus, the displacement signal measured by the X detector can be simply expressed as $D_X(t) = \Delta m_x(t) + \Delta n_x(t) = \Delta m(t) \sin(\phi) + \Delta n(t) \cos(\phi)$ (ϕ is the angle between the y detection axis and the minimum eigenfrequency direction of the radial motion), and the signal from the Y detector is $D_Y(t) = \Delta m(t) \cos(\phi) + \Delta n(t) \sin(\phi)$. Thus, the displacement power spectra can be expressed as $S_X = |D_X(f)|^2 = |\Delta m(f)|^2 \sin^2(\phi) + |\Delta n(f)|^2 \cos^2(\phi)$, and $S_Y = |\Delta m(f)|^2 \cos^2(\phi) + |\Delta n(f)|^2 \sin^2(\phi)$.

The spot size of the trapping laser before the objective lens was measured by a beam profiler with $2w_{x_0} \times 2w_{y_0} = 3.38 \text{ mm} \times 3.16 \text{ mm}$. The x measurement axis was aligned with the radial major axis of the incident beam, and the y detection axis was vertical to the major axis. As a result, the X detector measured a maximum eigenfrequency of 122.1 kHz, and the Y detector obtained a minimum eigenfrequency of 89.0 kHz when the linear polarization was along the minor (y) axis of the incident beam, as shown in Fig. 3(d). Because the detection systems were fixed, the detectors measured the projections of the motions. The radial eigenfrequencies were periodically changed with the rotation of the linear polarization [Fig. 3(e)]. Simultaneously, the peak heights of the power spectra were changed. The measured maximum frequency differences were 8.3 and 6.1 kHz in the two eigendirections measured. We also examined the circularly polarized light field. The measured eigenfrequencies in the radial direction were 107.6 kHz on the x axis and 98.7 kHz on the y axis, which are located between the two eigenfrequencies for the linear polarization case, as shown in Fig. 3(e). Here, we only consider the case that the size of the particle is much smaller than the wavelength of trapping laser, so the Rayleigh approximation is effective. Four different sizes ($\sim 190, 100, 90, 80$ nm) of nanoparticles from different batches of two companies of microspheres (Tianjin BaseLine ChromTech Research Centre and Ningbo Jinlei Nanomaterials Technology Co., Ltd.) were measured, which showed a similar polarization effect.

Finally, we demonstrate that some effects could be enhanced or canceled by controlling the relative orientation and ellipticity of the two ellipses' parameters. Due to elliptical TEM₀₀-mode Gaussian beam, the radial eigenfrequencies are nondegenerate for the circularly polarized light field. By choosing an appropriate elliptical polarization and the orientation relative to the elliptical TEM₀₀-mode Gaussian beam, we made the two radial motions degenerate in the experiment, as illustrated in the middle plot of Fig. 5. The radial eigenfrequency becomes 104.0 kHz. When the linear polarization is aligned along the short axis of the elliptical TEM₀₀-mode

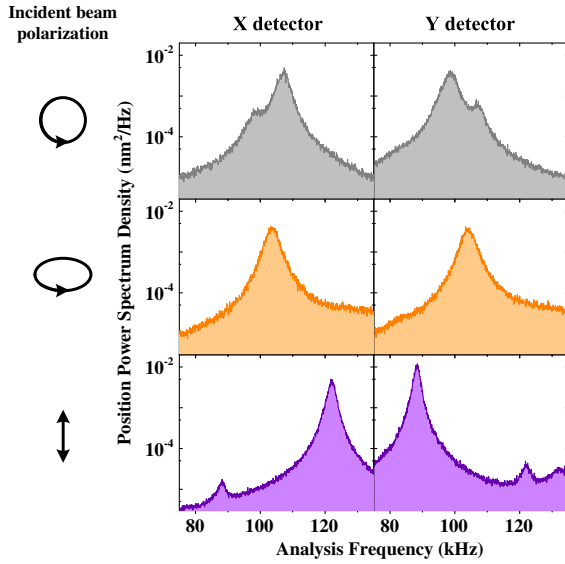


Fig. 5. Difference of two radial eigenfrequencies is enhanced or canceled by controlling the relative orientation and ellipticity of the two ellipses. The long axis of the elliptical TEM₀₀-mode Gaussian beam is at the x_0 axis. The air pressure during the measurements was 300 Pa, RBW = 10 Hz, VBW = 10 Hz.

Gaussian beam, the difference of two radial eigenfrequencies become maximum, as shown in the bottom plot of Fig. 5.

4. CONCLUSION

In conclusion, this study explores the polarization influence of a TEM₀₀-mode Gaussian trapping laser with a slightly elliptical profile on the center-of-mass translational motion of an optically levitated nanosphere. The power spectra of the motion are measured, and the motions in the radial direction

APPENDIX A: THEORETICAL CALCULATIONS OF FIELD COMPONENTS IN THE FOCUS REGION

In this section, we use the angular spectrum representation to calculate the field distribution in the focus region. The incident beam at the $z_0 = 0$ plane in the angular spectrum representation can be expressed as

$$A_{\text{in}}(\alpha, \beta) = \left(\frac{1}{2\pi}\right)^2 \iint_{-\infty}^{\infty} E_{\text{in}}(x_0, y_0, 0) \exp\{-ik \sin(\alpha)[x_0 \cos(\beta) - y_0 \sin(\beta)]\} dx_0 dy_0. \quad (\text{A1})$$

In the experiment, the incident field is a TEM₀₀-mode Gaussian beam, but usually with a slightly elliptical profile. The amplitude of the incident field can be written as

$$E_{\text{in}}(x_0, y_0, 0) = E_0 e^{-\left(\frac{x_0^2}{w_{0x}^2} + \frac{y_0^2}{w_{0y}^2}\right)}. \quad (\text{A2})$$

Thus, in a spherical coordinate system, neglecting the fixed phase term, the incident field mode at a reference surface can be written as

$$A_{\text{in}}(\alpha, \beta) = E_0 e^{-f^2 \sin^2(\alpha) \left(\frac{\cos^2(\beta)}{w_{0x}^2} + \frac{\sin^2(\beta)}{w_{0y}^2}\right)}, \quad (\text{A3})$$

where f is the distance from the field point to the reference surface. If $\delta = (w_{0x} - w_{0y})/w_{0x} = 0$, this corresponds to a circular Gaussian beam; thus,

$$A_{\text{in}}(\alpha, \beta) = E_0 e^{-\frac{f^2 \sin^2(\alpha)}{w_{0x}^2}}. \quad (\text{A4})$$

If $0 < \delta \ll 1$, the first-order approximation can be obtained as follows:

$$A_{\text{in}}(\alpha, \beta) \approx E_0 \left[1 - 2 \frac{f^2 \sin^2(\alpha)}{w_{0x}^2} \sin^2(\beta) \delta\right] e^{-\frac{f^2 \sin^2(\alpha)}{w_{0x}^2}}. \quad (\text{A5})$$

It can be seen that this formula is an ideal TEM₀₀-mode Gaussian beam with a small modification. The transformation matrix [41,46] of the aplanatic lens is

$$C_M = \begin{pmatrix} 1 + [\cos(\alpha) - 1]\cos^2(\beta) & [\cos(\alpha) - 1]\cos(\beta)\sin(\beta) & -\sin(\alpha)\cos(\beta) \\ \cos(\beta)\sin(\beta)[\cos(\alpha) - 1] & 1 + [\cos(\alpha) - 1]\sin^2(\beta) & -\sin(\alpha)\cos(\beta) \\ \sin(\alpha)\cos(\beta) & \sin(\alpha)\sin(\beta) & \cos(\alpha) \end{pmatrix}. \quad (\text{A6})$$

show different characteristics that depend on the relative orientation and ellipticity of the two ellipses' parameters. The results are consistent with the predictions of vector diffraction theory. This study provides a method for manipulating the optically levitated nanosphere; moreover, it can aid in evaluating a tightly focused laser profile using the motion of a nanosphere.

According to the relation of the first-kind n th-order Bessel function [46],

$$\int_0^{2\pi} e^{i\sin\beta} e^{is\cos(\beta-\phi)} d\beta = 2\pi i^n J_n(s) e^{i\sin\phi}, \quad (\text{A7})$$

for linearly polarized incident light, by substituting Eqs. (A5)–(A7) into Eq. (1), we can obtain

$$\vec{E}(r, \phi, z) = \begin{pmatrix} \sin(\theta)(E_{00} - \delta E_{01} - \delta E_{02}) + (E_{20} - \delta E_{22}) \sin(\theta + 2\phi) - \delta E_{21} \sin(\theta) \cos(2\phi) \\ \cos(\theta)(E_{00} - \delta E_{01} + \delta E_{02}) - (E_{20} - \delta E_{22}) \cos(\theta + 2\phi) - \delta E_{21} \cos(\theta) \cos(2\phi) \\ 2iE_{10} \sin(\theta + \phi) - i\delta E_{11}[2 \sin(\theta + \phi) - \sin(\theta - \phi)] \end{pmatrix}, \quad (\text{A8})$$

where θ is the angle between the polarization and the y_0 axis. The electric field terms are defined as follows:

$$E_{00}(r, z) = \int_0^{\alpha_0} E_{c1}(\alpha)[1 + \cos(\alpha)]J_0(s)d\alpha, \quad (\text{A9})$$

$$E_{01}(r, z) = \int_0^{\alpha_0} E_{c2}(\alpha)[1 + \cos(\alpha)]J_0(s)d\alpha, \quad (\text{A10})$$

$$E_{02}(r, z) = \int_0^{\alpha_0} \frac{E_{c2}}{2}[1 - \cos(\alpha)]J_0(s)d\alpha, \quad (\text{A11})$$

$$E_{10}(r, z) = \int_0^{\alpha_0} E_{c1}(\alpha) \sin(\alpha)J_1(s)d\alpha, \quad (\text{A12})$$

$$E_{11}(r, z) = \int_0^{\alpha_0} E_{c2}(\alpha) \sin(\alpha)J_1(s)d\alpha, \quad (\text{A13})$$

$$E_{20}(r, z) = \int_0^{\alpha_0} E_{c1}(\alpha)[1 - \cos(\alpha)]J_2(s)d\alpha, \quad (\text{A14})$$

$$E_{21}(r, z) = \int_0^{\alpha_0} E_{c2}(\alpha)[1 + \cos(\alpha)]J_2(s)d\alpha, \quad (\text{A15})$$

$$E_{22}(r, z) = \int_0^{\alpha_0} E_{c2}(\alpha)[1 - \cos(\alpha)]J_2(s)d\alpha, \quad (\text{A16})$$

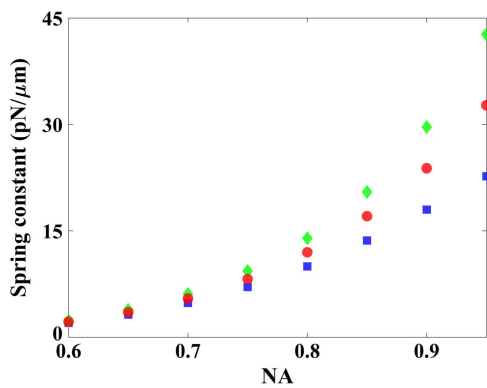


Fig. 6. Theoretical simulation of the radial spring constant versus the NA in the focus region when $\delta = 0$. Diamond and square symbols represent two eigendirections of a linearly polarized laser. Circles correspond to the results of the circularly polarized light.

where $s = kr \sin(\alpha)$, and

$$E_{c1}(\alpha) = iC\pi E_0 e^{-\frac{f^2 \sin^2(\alpha)}{w_{0x}^2}} \sqrt{\cos(\alpha)} \sin(\alpha) e^{ikz \cos(\alpha)}, \quad (\text{A17})$$

$$E_{c2}(\alpha) = \frac{f^2 \sin^2(\alpha)}{w_{0x}^2} E_{c1}(\alpha). \quad (\text{A18})$$

Thus, the intensity and gradient of the field can be easily obtained using the above equations. Numerical calculations of the radial spring constants are presented in Fig. 6 for $\delta = 0$. The radial spring constants for linear polarization are degenerate when NA is small, and equal to those of circular polarization. The splitting of the radial spring constants for linear polarization increases when the NA is increased. However, the spring constants for circular polarization keep degenerate, lying between the radial spring constants for linear polarization. We further consider the effect of the ellipticity of the incident field. Figure 7 illustrates the radial spring constants in the focus region as a function of the NA and δ for linearly and circularly polarized lasers. The ellipticity induces the splitting of the spring constant for the circular polarization, as seen in the red and light-red surfaces in Fig. 7. The radial spring constants periodically change with the rotation of linear polarization. The maximum and minimum values for the two spring constants are plotted. In Fig. 7, the green and light-green surfaces correspond to the large spring constant, while the blue and light-blue surfaces represent the small spring constant. The experimental

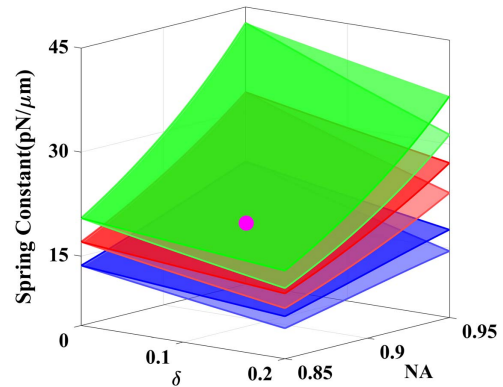


Fig. 7. Theoretical calculation of the radial spring constant in the focus region as a function of the NA and δ for linearly and circularly polarized lasers. Green and light-green surfaces represent maximum and minimum values of the large spring constant (eigenfrequency) for linear polarization. Blue and light-blue surfaces correspond to the small spring constant for linear polarization; red and light-red surfaces represent the case of a circularly polarized laser. The purple point corresponds to the experimental results in Figs. 3(d)–3(e).

results in Figs. 3(d)–3(e) are marked in Fig. 7 and correspond quantitatively to the theoretical calculations.

Funding. National Natural Science Foundation of China (11234008, 11361161002, 11654002, 61571276); National Key Research and Development Plan (2016YFA0301602); Research Project Supported by Shanxi Scholarship Council of China (2015-002).

REFERENCES

- A. Ashkin, "Acceleration and trapping of particles by radiation pressure," *Phys. Rev. Lett.* **24**, 156–159 (1970).
- B. Darquié, M. P. A. Jones, J. Dingjan, J. Beugnon, S. Bergamini, Y. Sortais, G. Messin, A. Browaeys, and P. Grangier, "Controlled single-photon emission from a single trapped two-level atom," *Science* **309**, 454–456 (2005).
- B. Liu, G. Jin, R. Sun, J. He, and J. Wang, "Measurement of magic-wavelength optical dipole trap by using the laser-induced fluorescence spectra of trapped single cesium atoms," *Opt. Express* **25**, 15861–15867 (2017).
- D. E. Chang, C. A. Regal, S. B. Papp, D. J. Wilson, J. Ye, O. Painter, H. J. Kimble, and P. Zoller, "Cavity opto-mechanics using an optically levitated nanosphere," *Proc. Natl. Acad. Sci. USA* **107**, 1005–1010 (2010).
- A. A. Geraci, S. B. Papp, and J. Kitching, "Short-range force detection using optically cooled levitated microspheres," *Phys. Rev. Lett.* **105**, 101101 (2010).
- J. Millen, T. Deesuwana, P. Barker, and J. Anders, "Nanoscale temperature measurements using non-equilibrium Brownian dynamics of a levitated nanosphere," *Nat. Nanotech.* **9**, 425–429 (2014).
- L. P. Neukirch, E. V. Haartman, J. M. Rosenholm, and A. N. Vamivakas, "Multi-dimensional single-spin nano-optomechanics with a levitated nanodiamond," *Nat. Photonics* **9**, 653–657 (2015).
- O. R. Isart, M. L. Juan, R. Quidant, and J. I. Cirac, "Toward quantum superposition of living organisms," *New J. Phys.* **12**, 033015 (2010).
- J. Li, I. M. Haghghi, N. Malossi, S. Zippilli, and D. Vitali, "Generation and detection of large and robust entanglement between two different mechanical resonators in cavity optomechanics," *New J. Phys.* **17**, 103037 (2015).
- A. Bassi, K. Lochan, S. Satin, T. P. Singh, and H. Ulbricht, "Models of wave-function collapse, underlying theories, and experimental tests," *Rev. Mod. Phys.* **85**, 471–527 (2013).
- P. F. Barker and M. N. Schneider, "Cavity cooling of an optically trapped nanoparticle," *Phys. Rev. A* **81**, 023826 (2010).
- T. Li, S. Kheifets, D. Medellin, and M. G. Raizen, "Measurement of the instantaneous velocity of a Brownian particle," *Science* **328**, 1673–1675 (2010).
- T. Li, S. Kheifets, and M. G. Raizen, "Millikelvin cooling of an optically trapped microsphere in vacuum," *Nat. Phys.* **7**, 527–530 (2011).
- J. Gieseler, B. Deutsch, R. Quidant, and L. Novotny, "Subkelvin parametric feedback cooling of a laser-trapped nanoparticle," *Phys. Rev. Lett.* **109**, 103603 (2012).
- M. Frimmer, J. Gieseler, and L. Novotny, "Cooling mechanical oscillators by coherent control," *Phys. Rev. Lett.* **117**, 163601 (2016).
- P. V. Ruijgrok, N. R. Verhart, P. Zijlstra, A. L. Tchebotareva, and M. Orrit, "Brownian fluctuations and heating of an optically aligned gold nanorod," *Phys. Rev. Lett.* **107**, 037401 (2011).
- Y. Arita, M. Mazilu, and K. Dholakia, "Laser-induced rotation and cooling of a trapped microgyroscope in vacuum," *Nat. Commun.* **4**, 2374 (2013).
- S. Kuhn, P. Asenbaum, A. Kosloff, M. Sclafani, B. A. Stickler, S. Nimrichter, K. Hornberger, O. Cheshnovsky, F. Patolsky, and M. Arndt, "Cavity-assisted manipulation of freely rotating silicon nanorods in high vacuum," *Nano. Lett.* **15**, 5604–5608 (2015).
- T. M. Hoang, Y. Ma, J. Ahn, J. Bang, F. Robicheaux, Z. Yin, and T. Li, "Torsional optomechanics of a levitated nonspherical nanoparticle," *Phys. Rev. Lett.* **117**, 123604 (2016).
- S. Kuhn, B. A. Stickler, A. Kosloff, F. Patolsky, K. Hornberger, M. Arndt, and J. Millen, "Optically driven ultra-stable nanomechanical rotor," *Nat. Commun.* **8**, 1670 (2017).
- V. Svak, O. Brzobohatý, M. Šiler, P. Jákl, J. Kaňka, P. Zemánek, and S. H. Simpson, "Transverse spin forces and non-equilibrium particle dynamics in a circularly polarized vacuum optical trap," *Nat. Commun.* **9**, 5453 (2018).
- R. Reimann, M. Doderer, E. Hebestreit, R. Diehl, M. Frimmer, D. Windey, F. Tebbenjohanns, and L. Novotny, "GHz rotation of an optically trapped nanoparticle in vacuum," *Phys. Rev. Lett.* **121**, 033602 (2018).
- J. Ahn, Z. Xu, J. Bang, Y. Deng, T. M. Hoang, Q. Han, R. Ma, and T. Li, "Optically levitated nanodumbbell torsion balance and GHz nanomechanical rotor," *Phys. Rev. Lett.* **121**, 033603 (2018).
- R. Zhao, A. Manjavacas, F. J. G. D. Abajo, and J. B. Pendry, "Rotational quantum friction," *Phys. Rev. Lett.* **109**, 123604 (2012).
- A. Manjavacas, F. J. R. Fortuño, F. J. G. D. Abajo, and A. V. Zayats, "Lateral Casimir force on a rotating particle near a planar surface," *Phys. Rev. Lett.* **118**, 133605 (2017).
- Z. Xu and T. Li, "Detecting Casimir torque with an optically levitated nanorod," *Phys. Rev. A* **96**, 033843 (2017).
- S. Bose, A. Mazumdar, G. W. Morley, H. Ulbricht, M. Toroš, M. Paternostro, A. A. Geraci, P. F. Barker, M. S. Kim, and G. Milburn, "Spin entanglement witness for quantum gravity," *Phys. Rev. Lett.* **119**, 240401 (2017).
- C. Marletto and V. Vedral, "Gravitationally induced entanglement between two massive particles is sufficient evidence of quantum effects in gravity," *Phys. Rev. Lett.* **119**, 240402 (2017).
- Y. Huang, T. Li, and Z. Yin, "Symmetry-breaking dynamics of the finite-size Lipkin-Meshkov-Glick model near ground state," *Phys. Rev. A* **97**, 012115 (2018).
- E. Wolf, "Electromagnetic diffraction in optical systems - I. An integral representation of the image field," *Proc. R. Soc. A* **253**, 349–357 (1959).
- B. Richards and E. Wolf, "Electromagnetic diffraction in optical systems - II. Structure of the image field in an aplanatic system," *Proc. R. Soc. A* **253**, 358–379 (1959).
- R. Dorn, S. Quabis, and G. Leuchs, "Sharper focus for a radially polarized light beam," *Phys. Rev. Lett.* **91**, 233901 (2003).
- L. M. Davis, "Theory of electromagnetic beams," *Phys. Rev. A* **19**, 1177–1179 (1979).
- A. Wünsche, "Transition from the paraxial approximation to exact solutions of the wave equation and application to Gaussian beams," *J. Opt. Soc. Am. A* **9**, 765–774 (1992).
- B. Lü and K. Duan, "Nonparaxial propagation of vectorial Gaussian beams diffracted at a circular aperture," *Opt. Lett.* **28**, 2440–2442 (2003).
- B. Huang, M. Bates, and X. Zhuang, "Super-resolution fluorescence microscopy," *Ann. Rev. Biochem.* **78**, 993–1016 (2009).
- G. Schnoering, L. V. Poulikakos, Y. R. Cabara, A. C. Durand, D. J. Norris, and C. Genet, "Three-dimensional enantiomeric recognition of optically trapped single chiral nanoparticles," *Phys. Rev. Lett.* **121**, 023902 (2018).
- M. T. Do, T. T. N. Nguyen, Q. Li, H. Benisty, I. L. Rak, and N. D. Lai, "Submicrometer 3D structures fabrication enabled by one-photon absorption direct laser writing," *Opt. Express* **21**, 20964–20973 (2013).
- E. Betzig and R. J. Chichester, "Single molecules observed by near-field scanning optical microscopy," *Science* **262**, 1422–1425 (1993).
- S. Quabis, R. Dorn, M. Eberler, O. Glöckl, and G. Leuchs, "Focusing light to a tighter spot," *Opt. Commun.* **179**, 1–7 (2000).
- X. Hao, C. Kuang, T. Wang, and X. Liu, "Effects of polarization on the de-excitation dark focal spot in STED microscopy," *J. Opt.* **12**, 115707 (2010).
- A. Ashkin, J. M. Dziedzic, J. E. Bjorkholm, and S. Chu, "Observation of a single-beam gradient force optical trap for dielectric particles," *Opt. Lett.* **11**, 288–290 (1986).
- R. Omori, T. Kobayashi, and A. Suzuki, "Observation of a single-beam gradient-force optical trap for dielectric particles in air," *Opt. Lett.* **22**, 816–818 (1997).

44. K. Duan and B. Lü, "Propagation properties of vectorial elliptical Gaussian beams beyond the paraxial approximation," *Opt. Laser Technol.* **36**, 489–496 (2004).
45. Y. Zhang, "Nonparaxial propagation analysis of elliptical Gaussian beams diffracted by a circular aperture," *Opt. Commun.* **248**, 317–326 (2005).
46. A. S. V. D. Nes, L. Billy, S. F. Pereira, and J. J. M. Braat, "Calculation of the vectorial field distribution in a stratified focal region of a high numerical aperture imaging system," *Opt. Express* **12**, 1281–1293 (2004).
47. Y. Jin, X. Yu, and J. Zhang, "Optically levitated nanosphere with high trapping frequency," *Sci. China Phys. Mech.* **61**, 114221 (2018).
48. Y. Harada and T. Asakura, "Radiation forces on a dielectric sphere in the Rayleigh scattering regime," *Opt. Commun.* **124**, 529–541 (1996).